INORGANIC CHEMISTRY FRONTIERS

CCS 中国化学会 CHINESE CHEMICAL SOCIETY

ROYAL SOCIETY OF CHEMISTRY

Low-Temperature Oxyl Transfer to Carbon Monoxide from Zn^{II}–Oxyl site in Zeolite Catalyst

Journal:	*Inorganic Chemistry Frontiers*
Manuscript ID	QI-RES-09-2020-001112.R2
Article Type:	Research Article
Date Submitted by the Author:	23-Oct-2020
Complete List of Authors:	Oda, Akira; Nagoya University, Department of Materials Chemistry Graduate School of Engineering Kumagai, Jun; Nagoya University, Institute of Materials and Systems for Surstainability Ohkubo, Takahiro; Okayama University, Department of Chemistry Kuroda, Yasushige; Okayama Daigaku, Department of Chemistry

ARTICLE

Low-Temperature Oxyl Transfer to Carbon Monoxide from Zn^{II}–Oxyl site in Zeolite Catalyst

Akira Oda,*[a,b,c] Jun Kumagai,[d] Takahiro Ohkubo,[b] Yasushige Kuroda[b]

Received 00th January 20xx,
Accepted 00th January 20xx

DOI: 10.1039/x0xx00000x

The atomic O radical anion bound to a metal ion (metal–oxyl) is a key intermediate in a variety of oxidative reactions. Understanding of its structure-reactivity relationship is highly desirable for the rational design of challenging oxidative transformation processes. However, due to the difficulty of analysis, even the identification of oxyl is a challenging subject especially in the research field of the heterogeneous catalyst. Here, we newly report a low-temperature oxyl transfer to CO from the Zn^{II}–oxyl bond isolated in the zeolite catalyst. Zeolite matrix isolation of the novel Zn^{II}–oxyl bond allows us to observe unique spectroscopic probes of oxyl: vibronically-resolved spectrum and ESR signatures. Using the oxyl-selective spectroscopic probes, we successfully demonstrated that the Zn^{II}–oxyl bond has a capability for transferring the oxyl to CO even at 150 K with the generation of a single $Zn^{I\bullet}$ species. The superhyperfine interaction of the $Zn^{I\bullet}$ species with the framework Al atom, observed upon the oxyl-transfer reaction, provided the direct experimental evidence that the oxyl-functionality emerged at the framework Al site. DFT calculations showed that the Zn^{II}–oxyl bond, that is constrained by the zeolite lattice ligation, acts as a superior electron donor toward CO at the rate-determining step in the oxyl-transfer reaction and effectively reduces the barrier to be < 5 kJ mol^{-1}. Based on the results obtained in the present study as well as the previous work, we further deepen the understanding of why the abnormal Zn^{II}–oxyl bond having exceptional reactivities is created by the zeolite lattice ligation.

Introduction

It has been suggested since the 1980s that solid surfaces generate an atomic oxygen radical anion (oxyl) as the transient reactive site capable of challenging oxidative reactions, e.g., methane partial oxidation.[1-11] The pioneer worker is Lunsford who developed several heterogeneous catalysts enabling the low-temperature partial oxidation of CH_4 and rationalized, for the first time, their exceptional reactivities by considering the in-situ generation of the transient surface oxyl.[1-5] Understanding of the structure-reactivity relationship of surface oxyls is highly desirable for the rational design of the next-generation heterogeneous catalysts for extremely difficult oxidative reactions. However, due to the difficulty of analysis, even the identification of oxyl is a challenging subject in the research field of the heterogeneous catalyst. It is difficult to obtain a clear ESR signal attributed to the opened electronic structure of oxyl due to its fast relaxation behaviour.[1, 4, 7, 12] Although it has been suggested that ultrafast IR spectroscopy may be able to analyse the surroundings of transient surface oxyl, there is no example of direct detection of metal–oxyl bonds by IR spectroscopy.[13, 14] Therefore, the fundamental information for the understanding of the structure-reactivity relationship of *surface oxyl* is critically lacking.

Recently, we have reported the oxyl bound to Zn^{II} in the zeolite catalyst.[15, 16] This is the first zinc oxide having a stable Zn^{II}–$O^{-\bullet}$ bond. The successful isolation of the novel Zn^{II}–$O^{-\bullet}$ bond within the zeolite matrix allowed us to observe unique spectroscopic probes of the oxyl: (1) near-IR vibronic progression associated with the Zn^{II}–oxyl vibrational stretching mode; (2) an axial ESR signal derived from the hole of $O^{-\bullet}$.[15, 16] Using these oxyl-selective spectroscopic probes, we were able to selectively examine the reactivity of the Zn^{II}–oxyl bond toward CH_4 and demonstrate that H-atom abstraction from CH_4 proceeds at oxyl even at RT to afford the methoxide that is converted to methanol by the subsequent H_2O-assisted extraction.[16] Based on the combined spectroscopic and computational study of the geometric and electronic structures of the Zn^{II}–oxyl bond, we have postulated that the zeolite-lattice ligation is indispensable for its exceptional state and reactivity.

Fundamental bonding question regarding the unprecedented Zn^{II}–oxyl bond motivates us to further explore its exceptional reactivity. The purpose of this study is to develop an understanding of the correlation among the local geometry, electronic state, and reactivity of the Zn^{II}–oxyl bond. Here, we newly report a combined spectroscopic and computational study of the oxyl transfer from the Zn^{II}–oxyl species to CO. Low-

[a]*Precursory Research for Embryonic Science and Technology, Japan Science and Technology Agency, Saitama 332-0012, Japan.*
[b]*Department of Chemistry, Graduate School of Natural Science and Technology, Okayama University, Okayama 700-8530, Japan.*
[c]*Department of Materials Chemistry, Graduate School of Engineering, Nagoya University, Nagoya 464-8603, Japan.*
[d]*Institute of Materials and System for Sustainability, Nagoya University, Nagoya 464-8601, Japan.*
† Footnotes relating to the title and/or authors should appear here.
Electronic Supplementary Information (ESI) available: [details of any supplementary information available should be included here]. See DOI: 10.1039/x0xx00000x

temperature oxidation of CO has a significant number of potential applications such as air purification, pollution control, and fuel gas purification.[17-19] It has been recognized that oxyl is one of the important reaction intermediate required for the low-temperature oxidation of CO; however, the detailed study has been limited in the gas phase experiments using the short-lived metal-oxyl cluster ions as the model species representing the local structure of the surface oxyls over heterogeneous catalysts.[20-25] The present study demonstrates that the Zn^{II}–oxyl species has a capability for transferring the oxyl to CO even at 150 K with the formation of a single $Zn^{I\bullet}$ site having the paramagnetic property. The site-correlation with the H-atom abstraction from CH_4 is spectroscopically ascertained. The superhyperfine interaction of the $Zn^{I\bullet}$ species with the framework Al atom, observed upon the oxyl-transfer reaction, provides first experimental evidence that the oxyl-functionalities emerged at the framework Al site. DFT calculations show that the Zn^{II}–oxyl bond, that is constrained by the zeolite lattice ligation, acts as an electron donor toward CO at the rate-determining step in the oxyl-transfer reaction and effectively reduces the barrier to be < 5 kJ mol^{-1}. Based on the results obtained in the present study as well as the previous work, we further deepen the understanding of why the abnormal Zn^{II}–oxyl bond having exceptional reactivities is created by the zeolite lattice ligation.

2. Experimental and Computational Methods

2.1. Sample Preparation. Zn^{II}–oxyl containing sample was prepared through the procedures developed in our previous work.[15, 16] Zn^{II} ion-exchanged MFI (Zn^{II}-MFI) with Si/Al = 11.9 and Zn/Al = 0.48 was obtained by the liquid-phase ion-exchange method, where the Na-MFI (Tosoh Co.) was used as the start material and $Zn(NO_3)_2$ (99%: Nacalai Tesque Inc.) aqueous solution was used as the Zn^{II} source. The Zn^{II}–MFI sample was activated by evacuation at 873 K, followed by treated with H_2 (99.99%: GL Sciences Co.) at 423 K.[15, 16, 26-28] Then, heterolytic cleavage of H_2 proceeds on the single Zn^{II} site, resulting in the generation of both Brønsted acid site and Zn^{II}–H site. After the preparation of the Zn^{II}–H species, the sample was irradiated with UV light in the presence of O_2 (99.9%: GL Sciences Co.). In this process, the photoreaction of Zn^{II}–H with O_2 proceeds, resulting in the generation of Zn^{II}–(O_3). By evacuation of the O_2 gas, the Zn^{II}–(O_3) was decomposed into Zn^{II}–oxyl with the liberation of O_2. In the present study, we examined its reactivity for CO (99.9%: GL Sciences Co.) at RT.

2.2. In Situ Ultra-Violet-Near Infrared (UV-Vis-NIR) Spectroscopy. UV−Vis−NIR diffuse reflectance (DR) spectra were recorded at RT in the wavelength range of 200−1000 nm with a 0.5 nm resolution using a spectrophotometer (JASCO V-570) equipped with an integral sphere attachment. Spectralon (Labsphere, USA) was used as the reference material. The sample was placed at the in situ cell made of fumed silica, which allows us not only to activate the sample at higher-temperature under the atmosphere of interest but also to measure the spectrum under in situ conditions.

2.3. In Situ Electron Spin Resonance (ESR) Spectroscopy. The X-band ESR spectra (ca. 9.0 GHz) were recorded at 4 K using a JEOL JESFA200 spectrometer equipped with a lower-temperature variable apparatus (ES-CT470). The sample was placed at the in situ cell made of fumed silica, which allows us not only to activate the sample at higher-temperature under the atmosphere of interest but also to measure the spectrum under in situ conditions. ESR simulations were conducted using Easyspin software.[29]

2.4. DFT calculations. 2.4.1. Model. All the calculations were performed using Gaussian 09 software.[30] A hybrid quantum mechanics/molecular mechanics (QM/MM) was employed to examine the reactivity of the Zn^{II}–oxyl site to CO.[30] The validity of this method has been verified in our previous work.[16] The MFI framework, which consists of 624-tetradedra sites, was constructed based on the crystal structure of the MFI zeolite.[31] The QM region consists of the Zn^{II}–oxyl species motif, the single framework Al site ($Al_1Si_4O_4$), and CO molecule. The remaining atoms were treated with a MM method. Electron embedding has been incorporated to provide a better explanation of the electrostatic interaction between the QM and MM regions. A B3LYP functional with a def2-TZVP basis set was used for calculations of the QM region. The UFF approach has been applied to the MM region, which reproduces the confinement effect of the zeolite pore structure on the reaction process.[16,32] Only the QM region has been optimized; the MM region has been fixed to maintain the crystallographic position of the zeolite framework atoms. The charges of the QM and MM regions were set to 0, respectively. The spin multiplicities of the QM and MM regions were set to 2, because the ground state of the Zn^{II}–oxyl site was the doublet spin state. The negligible dependency of theoretical results on the functional and the QM region size was confirmed in previous work.[16]

2.4.2. Calculation of Oxyl Transfer from Zn^{II}–Oxyl to CO. The transition state (TS) of oxyl transfer from Zn^{II}–oxyl to CO was searched using a *TS* keyword. The obtained TS geometry shows one imaginary frequency of the vibrational mode relevant to the oxyl- and CO-motions, from which we confirmed that the obtained TS geometry is accurate. The reaction routes were predicted by intrinsic reaction coordinate (IRC) calculations using the optimized TS geometry as the initial coordinate. To get as fine and accurate potential energy surface (PES) as possible, we performed the IRC calculations with a step size of 0.1 Bohr, where 300 points were examined along both the reaction routes. The relative self-consistent field (SCF) energies were calculated based on the total SCF energies of the free CO molecule and Zn^{II}–oxyl model. The zero-point energy (ZPE) correction was not considered in the PES to avoid the high-cost calculations. We made ZPE corrections only on the selected geometries, i.e., models **a, TS, b, c** in **Fig. 5A**. The optimized geometries of reactants and products had no imaginary vibrational mode, which indicates that these geometries were correctly optimized.

2.4.3. Simulation of Change in UV-Vis-NIR Spectra upon the Reaction. The UV-Vis-NIR spectrum of the $Zn^{I\bullet}$ model was

computed by the time-dependent (TD) method. The vibronic progression of Zn^{II}–oxyl was simulated by the procedures developed in our previous works: TD-based Franck Condon analyses.[15, 16, 33, 34] The fully-optimized coordinates of the QM regions were used as the candidate models. All the calculations were performed at the B3LYP/def2tzvp level.

3. Results

The Zn^{II}–oxyl species containing MFI zeolite was synthesized by the procedure previously developed by us.[15, 16] It has already been proven that there are at least three dominant types of the zinc species in the present sample: mononuclear Zn^{II}, Zn^{II}–superoxo, and Zn^{II}–oxyl species.[15, 16] In our efforts to understand how reactive the Zn^{II}–oxyl species would be toward the CO molecule, the change in the state of the Zn^{II}–oxyl species upon the reaction with CO was monitored by X-band ESR and UV-Vis-NIR spectroscopies.

The ESR signature of the Zn^{II}–oxyl site can be observed only at low temperature (4 K).[15, 16] Therefore, the ESR tube filled with the Zn^{II}–oxyl containing sample was cooled to 4 K, and then the sample was exposed to the very small amount of CO (responsible for P_e < 0.1 Torr at RT) at 4 K. Subsequently, the sample was heated to reaction temperatures (100–200 K) and left at these temperatures for 10 minutes. After cooling to 4 K again, the ESR measurements were performed to examine the change in the Zn^{II}–oxyl signal, through which the low-temperature reactivity of the Zn^{II}–oxyl site to CO was examined selectively.

Fig. 1 shows the change in the ESR spectrum of the sample upon the reaction with CO at low temperatures (100–200 K). Looking at the spectrum of the sample before heating to the reaction temperatures (red line: 4 K), it can be seen that two types of ESR signals are observed. As demonstrated by our previous work, these are derived from the Zn^{II}–oxyl and Zn^{II}–superoxo species.[15, 16] For clarity, these ESR features were marked with "Zn^{II}–oxyl" and "Zn^{II}–superoxo" in the figure. At first glance, the proportion of the Zn^{II}–superoxo species seems to be relatively high, but this is not the truth. The ESR signal of the Zn^{II}–oxyl species is significantly broadened; its intensity is ≈100 times smaller than the intensity of the ESR signal of the corresponding precursor, i.e., Zn^{II}–ozonide.[15, 16] This is due to the fast relaxation behavior of oxyl having the near-degenerate orbitals, i.e., singly occupied oxyl-2p_x and doubly occupied oxyl-2p_y orbitals.[15, 16]

Even if the sample was heated to 100 K, the intensity of the oxyl ESR signal hardly changed (**Fig. 1,** pink line), which indicates no reaction with CO at this temperature. However, the intensity of the oxyl-derived ESR signal significantly decreased at around 150 K, and disappeared at 200 K (**Fig. 1,** purple and blue lines). These are spectroscopic evidence for the low-temperature reaction of the Zn^{II}–oxyl species with CO. In parallel with the decrease in the ESR signature of the Zn^{II}–oxyl species, the development of the distinct ESR signal was observed at around the centre-field. Based on the ESR simulations, the *g*-tenor was determined as g_{xx}= 1.9952, g_{yy}= 1.9982, g_{zz}= 2.0014. This ESR feature can be assigned as the paramagnetic $Zn^{I\bullet}$ site.[35-41] These spectral changes can be interpreted by considering that the Zn^{II}–oxyl species transferred its oxyl to CO at around 150 K and generated the paramagnetic $Zn^{I\bullet}$ species (**Scheme 1**). It is worth noting that the intensity of the ESR signal derived from superoxo hardly changed. Therefore, the possibility of the involvement of the Zn^{II}–superoxo in the reaction can be excluded from the consideration.

The characteristics of the ESR signal of the generated $Zn^{I\bullet}$ species are summarized in **Fig. 2**, where **Fig. 2A** shows an enlarged view of the 1500–5000 G region, whereas **Fig. 2B** shows an enlarged view of the 3235–3260 G area. From **Fig. 2A**, we can see that the six-lines pattern appeared in a 1500–5000 G region. This signal is due to the hyperfine interaction of the $^{67}Zn^{I\bullet}$ species (I = 5/2; a natural abundance: ca. 4%).[35, 36] The ESR simulation has confirmed the large hyperfine splitting with A_{xx}= 537, A_{yy}= 541, A_{zz}= 547 G tensor (**Fig. 2A, red line**), which correlates well with the previously reported hyperfine splitting observed for the $^{67}Zn^{I\bullet}$ species in the γ-irradicated calcite.[42] An increase in the intensity of the $^{67}Zn^{I\bullet}$ hyperfine structure has been confirmed during the low-temperature reaction with CO (**Fig. 1, enlarged views of the 2400–3000 G and 3600–3800 G regions; see the ESR signals marked as "$^{67}Zn^{I\bullet}$"**). Therefore, there is no doubt that the $Zn^{I\bullet}$ species is produced during the low-temperature reaction of the Zn^{II}–oxyl species with CO via the oxyl transfer. Despite the low resolution, another type of the hyperfine structure was also observed in the 3235–3260 G region (**Fig. 2B**). Recently, Morra et al. have employed ESR and hyperfine sublevel correlation (HYSCORE) spectroscopy at X- and Q-band frequencies for characterization of the $Zn^{I\bullet}$ modified MFI zeolite that prepared through the solid-state ion-exchange using zero-valent zinc vapor as the zinc source, and observed the superhyperfine interaction of the $Zn^{I\bullet}$ species with a ^{27}Al atom (I = 5/2).[40] More recently, ^{17}O-hyperfine structures of the ^{17}O-labelled zeolite lattice ligating the $Zn^{I\bullet}$ species have been reported by the same group.[41] From these findings, Morra et al. has demonstrated, for the first time, the paramagnetic $Zn^{I\bullet}$ species is stabilized via interactions with the lattice oxygens connected to the framework Al atom. Although the resolution of the superhyperfine structure observed by the X-band ESR measurement in the present study is not well-resolved to analyse in detail, a good correlation with the Morra's data was confirmed by the simulation assuming the g_x= 1.9952, g_y= 1.9982, g_z= 2.0014 and A_x= 1.04, A_y= 1.09, A_z= 1.39 G tensors (**Fig. 2B, red line**).[40] Since the superhyperfine structure arises due to the distribution of an unpaired electron from the Zn radical to the nucleus (Al), the good correlation indicates that the paramagnetic $Zn^{I\bullet}$ species, even in the present case, is generated near the framework Al site. We have recently developed the model of the Zn^{II}–oxyl bond.[15, 16] This model features the Zn^{II} ion adopting the inverse Y-shaped structure via interactions with a terminal oxyl and two lattice oxygens connected to the framework Al atom. If oxyl is transferred to CO with the generation of the $Zn^{I\bullet}$ species on the framework Al site, as shown in **Scheme 1**, the experimental observation of the $Zn^{I\bullet}$–^{27}Al superhyperfine structure is valid.

To further support the oxyl transfer reaction, the change in the state of the Zn^{II}–oxyl site upon the reaction with CO was monitored by UV-Vis-NIR spectroscopy. Our UV-Vis-NIR equipment cannot directly trace the reaction below RT; however, the experimental data, that further supports the oxyl-transfer reaction, could be obtained by the UV-Vis-NIR measurements at RT, and thereby the details are described below.

The UV-Vis-NIR spectrum of the oxyl-containing sample, that was collected under vacuum at RT, was shown in **Fig. 3A** as a red line. The Zn^{II}–oxyl site exhibits the small peaks in the near-IR region. These are derived from the vibronic progression associated with the Zn^{II}–oxyl vibrational mode.[15, 16] This vibronic progression is peculiar to the Zn^{II}–oxyl bond isolated in the zeolite matrix; thus, it can be used as the spectroscopic probe to selectively examine the reactivity of the Zn^{II}–oxyl species toward CO. The change in the state of the Zn^{II}–oxyl species upon the reaction with CO was monitored by the UV-Vis-NIR spectroscopy. With increasing the amount of the introduction of CO (P_e < 0.01 Torr), the intensity of the near-IR vibronic progression gradually decreased (**Fig. 3A, red line→blue line)**, indicating the occurrence of the reaction between the oxyl with CO. Upon this reaction, the distinct UV bands appeared at 218, 246, and 306 nm, and these intensities increased with increasing the introduction amounts of CO. **Fig. 3B** represents a plot of the change in the intensity of the UV-band at 307 nm against that of the 832 nm band of the near-IR vibronic progression. A linear relationship was confirmed between them. This is the experimental evidence that the UV-bands are attributed to the species that is generated upon the reaction of Zn^{II}–oxyl site with CO at RT. Taking account of the reaction mechanism developed by the low-temperature ESR spectroscopy (**Scheme 1**), the three UV-bands are assignable to the paramagnetic $Zn^{I\bullet}$ species. In recent years, we have reported the process of the formation of the paramagnetic $Zn^{I\bullet}$ species through the photo-activation of the single Zn^0 atom or diamagnetic $[Zn^I–Zn^I]^{2+}$ species encapsulated within the zeolite cavity.[37, 39] In these processes, several broad absorption bands were observed in the UV-region and assigned as the 4*s*-4*p* transitions of the paramagnetic $Zn^{I\bullet}$ species. Experimental facts that common absorption bands were observed during the reaction with CO further supports the formation of the paramagnetic $Zn^{I\bullet}$ species through the oxyl-transfer from the Zn^{II}–oxyl to CO.

To further probe the reactive center hypothesis, we performed additional experiments where Zn^{II}–oxyl site was first deactivated by irreversible reaction with CH_4 and then reacted with CO. Our previous work has shown that the Zn^{II}–oxyl species enables H-atom abstraction from CH_4 to afford Zn^{II}–OH and Zn^{II}–OCH_3 even at RT.[16] It is the reactivity peculiar to the Zn^{II}–oxyl species; the spectator sites co-present in the present sample, i.e., single Zn^{II} and Zn^{II}–superoxo sites, are not involved in the RT activation of CH_4.[16] This oxyl-mediated H-atom abstraction from CH_4 is irreversible; in other words, the Zn^{II}–oxyl site is selectively deactivated through the reaction with CH_4. To further support that the low-temperature CO oxidation uniquely occurs at the Zn^{II}–oxyl site, we used CH_4 as a probe molecule; we further explored the oxygen transfer reactivity of the sample pretreated with CH_4 at RT.

First, the oxyl-containing sample was exposed to the CH_4 gas at RT, and subsequently evacuated at RT. After that, the sample was exposed to CO, and the ESR and UV-Vis-NIR spectra were collected. In contrast to the case for the sample not prereacted with CH_4, the spectroscopic fingerprints of the $Zn^{I\bullet}$ species, i.e., the distinct ESR signal at around the centre field and three UV-bands were not observed (**Fig. 4**, red lines). These results can be interpreted by considering that the Zn^{II}–oxyl species, that is deactivated through the pre-reaction with CH_4 at RT, is indispensable for the RT activation of CO; contributions of the spectator sites, i.e., the Zn^{II}–superoxo and mononuclear Zn^{II} species can be eliminated from the consideration.

A combination of UV-Vis-NIR and ESR spectroscopies provided experimental evidence that the Zn^{II}–oxyl species has a capability for transferring the oxyl to CO even at ca. 150 K. To further probe the exceptional reactivity of oxyl, we performed DFT calculations. Based on the previous work, we constructed the DFT cluster model of the Zn^{II}–oxyl site.[15, 16] **Fig. 5A** shows the computed potential energy surface (PES) of the oxyl transfer to CO. The doublet spin surface PES with low activation energy was computationally predicted. The ZPE-corrected barrier was 3.7 kJ mol^{-1}. The computationally predicted exothermic reaction pathway that requires only a 3.7 kJ mol^{-1} barrier is not inconsistent with the observable result for the low-temperature oxyl transfer.

To validate our calculated lowest-energy geometries as well as the reaction mechanism, the change in spectrum upon the reaction was simulated and compared with the experimental data. Such a comparison allows us to evaluate the accuracy of the computationally proposed reaction mechanism.[15, 16, 33, 34] **Fig. 5B** shows the computed UV-Vis-NIR spectra of the reactant (Zn^{II}–oxyl species) and product ($Zn^{I\bullet}$ species). The Zn^{II}–oxyl model provided the relatively weak near-IR vibronic progression attributed to the stretching Zn^{II}–oxyl vibrational structure associated with the excitation from the doubly occupied σ bonding orbital to the singly occupied *nb* orbital, i.e., the localized oxyl-2*p* orbital perpendicular to the Zn^{II}–oxyl bond axis.[15, 16] On the other hand, the $Zn^{I\bullet}$ site provided the three distinct UV-bands attributed to the orbitally-allowed Zn-4*s* → Zn-4p_x, -4p_y, and 4p_z orbitals.[37] The spectral features, i.e., the band positions and relative intensities, were well correlated with the experimental data (**Fig. 3**). The successful simulation of the experimental data provided the experimental evidence that our models are correct; oxygen transfer reaction proceeds at the Zn^{II}–oxyl anchored on the single framework Al site through the reaction mechanism described in **Fig. 5A**.

We obtained computational models that exactly describe changes in the geometric and electronic structures of Zn^{II}–oxyl bond upon the reaction, which helps us to understand how Zn^{II}–oxyl bond enables low-temperature oxyl transfer to CO. As shown in **Fig. 5A**, CO first interacts with the Zn ion to generate the encounter complex (model **a**). In this stage, the Zn^{II}–oxyl state is maintained, as evidenced by the (1.00e) spin density

localized at the terminal oxygen atom. With an only 3.7 kJ mol^{-1} barrier, the CO molecule approaches to oxyl, resulting in the partial spin transfer from oxyl to CO (model **TS**). After that, the short oxyl–CO bond (1.307 Å) is formed (model **b**). This intermediate features the bent O–C–O core (136.3°). Since the spin density is distributed into the anti-bonding π_{O-C-O} orbital, this intermediate is assignable to the CO_2 radical anion bound to the Zn^{II} ion, i.e., Zn^{II}–($CO_2^{-\bullet}$) species. Finally, this CO_2 radical anion donates an electron to Zn^{II} ion to form a linear CO_2 molecule and the $Zn^{I\bullet}$ species with no activation energy (model **c**).

To further understand the electron flow mechanism, the Mulliken charges for Zn, O_t, C, and O atoms of **models a, b, c, and TS** were calculated (**Table 1**). It can be seen that the Mulliken charge of O_t increases in the process from **models TS** to **b (-**0.376 → 0.298**)**. This can be interpreted by considering the occurrence of the electron donation from O_t to CO with the generation of the Zn^{II}–($CO_2^{-\bullet}$) species. Upon the process from **models b** to **c**, the Mulliken charge of Zn decreases significantly (0.558 → 0.378). This is because the $CO_2^{-\bullet}$ species donates its electron to Zn^{II} with the generation of the $Zn^{I\bullet}$ species. Accordingly, the proposed electron flow mechanism was fully supported.

The rate-determining step is the oxyl–CO bond-forming process (model **TS**). As evidenced by the computed spin distribution of the model **TS** in **Fig. 5**, the unpaired electron was partially distributed from oxyl to CO; it is apparent that the singly-occupied (oxyl-2*p*)^1 orbital plays a pivotal role in the activation process. Here, a neutral CO molecule partially receives the electron density from the negatively charged oxyl to form the $[O\cdots CO]^{-\bullet}$ adduct. This electron transfer is the key interaction to facilitate the formation of the O–CO bond and thereby the oxyl transfer reaction.

Scheme 2 shows the schematic MO diagram representing how the oxyl-2*p* orbital interacts with frontier molecular orbitals (FMOs) of CO. The singly occupied oxyl-2*p* fragment orbital overlaps with the doubly occupied σ_{C-O} fragment orbital and unoccupied π^*_{C-O} fragment orbital, thereby forming three-centred MOs (σ_{O-CO}, nb_{O-CO}, and σ^*_{O-CO} orbitals). Three electrons are occupied in the generated three-centred MOs, resulting in the electron occupation pattern of $(\sigma_{O-CO})^2$ $(nb_{O-CO})^1$ $(\sigma^*_{O-CO})^0$. This electronic configuration imparts interatomic stability to the three centres (O–C–O). Through this interaction, i.e., three-centre three-electron (3c3e) interaction, the TS state becomes stable, and thereby oxyl-transfer reaction proceeds with a low barrier.

4. Discussion

The novel Zn^{II}–oxyl bond was isolated using a zeolite matrix. This *zeolite matrix isolation* allows us to observe unique spectroscopic probes of the Zn^{II}–oxyl bond: a vibronic progression and an ESR signature. Using such oxyl-selective spectroscopic probes, we explored the reactivity of the Zn^{II}–oxyl bond toward CO and revealed that the Zn^{II}–oxyl species has a capability for transferring the oxyl to CO with the generation of the paramagnetic $Zn^{I\bullet}$ species even at ca. 150 K.

Experimentally-supported DFT calculations showed that the Zn^{II}–oxyl bond, that is constrained by the zeolite lattice ligation, acts as a superior electron donor toward CO at the rate-determining step and effectively reduces the reaction barrier to be < 5 kJ mol^{-1}. The key feature of the Zn^{II}–oxyl species was its unpaired electron localized at oxyl; the constrained reactive (oxyl-2*p*)^1 orbital enables the stabilization of the TS geometry through the 3c3e interaction (**Scheme 2**).

In the previous work, we have demonstrated that oxyl acts as an electrophile at the transition state in the H-atom abstraction from CH_4.[16] Although the site-correlation between the oxyl-transfer and H-atom abstraction was unambiguously demonstrated by the present experiments, the roles of oxyl were entirely different. Given the low activation energies required for these reactions, i.e., < 10 kJ mol^{-1},[16] it is likely that the Zn^{II}–oxyl species has both the excellent electrophilicity and electron-donating property. It is surprising that such reactive species is observed experimentally. Therefore, understanding how the zeolite environment constrains the highly reactive Zn^{II}–oxyl bond is very significant from the viewpoint of catalyst design.

A $Zn^{I\bullet}$–^{27}Al superhyperfine structure, observed upon the oxyl-transfer reaction, provided first experimental evidence that the oxyl-functionalities emerged at the framework Al site. In other words, the negatively charged zeolite lattice oxygens function as the ligand for the Zn^{II} ion of the reactive Zn^{II}–oxyl species. This finding strengthened the previously-developed model of the Zn^{II}–oxyl species.[15, 16] The *zeolite-lattice ligation* constrains Zn into a +II charged state and imparts to Zn with very good acid properties, which plays a pivotal role in stabilizing the highly polarized Zn^{II}–$O^{-\bullet}$ bond.[15, 16] We have analysed the Zn^{II}–oxyl bonding mechanism through the Franck-Condon analyses on the vibronically-resolved spectrum associated to the Zn^{II}–oxyl vibrational structure in the $\boldsymbol{\sigma \rightarrow nb}$ (O-2*p*) excited state.[15, 16] This analysis has revealed that the $O^{-\bullet}$ interacts with Zn^{II} via only one $\boldsymbol{\sigma}$ bond, resulting in the reactive FMO, i.e., singly occupied O-2*p* orbital perpendicular to Zn^{II}–oxyl bond axis. The highly reactive FMOs of oxyl enables the stabilizations of the TS geometries in both the oxyl-transfer and H-atom abstraction from CH_4 through the 3c3e interaction with the FMOs of the respective substrates.[16] Accordingly, the exceptional reactivity of the Zn^{II}–oxyl revealed here can be considered to originate from the $O^{-\bullet}$ character specifically created by the zeolite-lattice ligation.

In coordination chemistry, many researchers have tried to isolate the stable metal–oxyl bonds to clarify the bonding nature, spectroscopic property, and reactivity of metal–oxyl bonds. So far, a handful of successful isolations of metal–oxyl bonds and intermediate metal–oxo/oxyl bonds has been reported.[43-49] It has been suggested that the controls of the electronic state of the metal–oxygen bond by using a ligand having electron-donating and/or -accepting properties are highly important for activating the metal–oxygen bonds.[45, 46] On the other hand, we have demonstrated that the metal–oxyl bond having exceptional reactivity toward CH_4 and CO can be stabilized through the electrostatic interaction with the zeolite-lattice oxygens having appropriate charges. Our finding newly suggests that we can

create metal–oxyl bonds by using charge-controlled lattice oxygens as the ligand to tune the polarization of the metal–oxygen bonds.

5. Conclusions

Using the oxyl-selective spectroscopic probes, we successfully demonstrated that the Zn^{II}–oxyl bond, isolated in a zeolite matrix, has a capability for transferring the oxyl to CO even at 150 K. The superhyperfine interaction of the $Zn^{I\bullet}$ species with the framework Al atom was observed upon the oxyl-transfer reaction, providing the direct experimental evidence that the oxyl-functionality emerged at the framework Al site. DFT calculations showed that the Zn^{II}–oxyl bond, that is constrained by the zeolite lattice ligation, acts as a superior electron donor toward CO at the rate-determining step and effectively reduces the reaction barrier to be < 5 kJ mol^{-1}. Combined with the previous reports, we further developed the basis of the structure-reactivity relationship of the Zn^{II}–oxyl bond and concluded that the exceptional reactivities of the Zn^{II}–oxyl bond can be considered to originate from the zeolite-lattice ligation. On these grounds, we suggest that metal-oxyl bonds can be created by using charge-controlled lattice oxygens as the ligand to tune the polarization of the metal–oxygen bonds. This concept is entirely different from the synthetic approach developed in coordination chemistry.

Conflicts of Interest

There are no conflicts to declare.

Acknowledgements

This work was supported by the JSPS Grant-in-Aid for Young Scientists (No. 20K15297), JSPS Grants-in-Aid for Scientific Research (B) (No. 16H04118), JSPS Grants-in-Aid for Challenging Exploratory (No. 21655021) and the JST PRESTO.

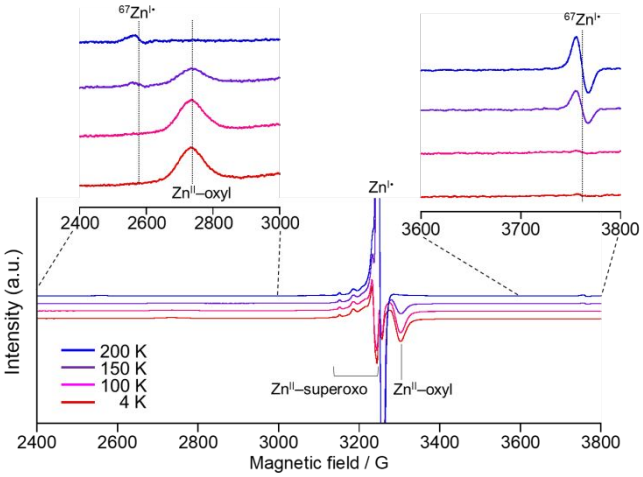

Fig. 1. In situ ESR spectra of the samples after the reaction with CO at 4 K, 100 K, 150 K, and 200 K for 10 minutes. All spectra were recorded at 4 K. The 2400–3000 G and 3600–3800 G regions were enlarged for clearly depicting the ESR signals of the Zn^{II}–oxyl and $Zn^{I\bullet}$ sites, where the offset of each spectrum was arbitrarily adjusted to make the peaks easier to see.

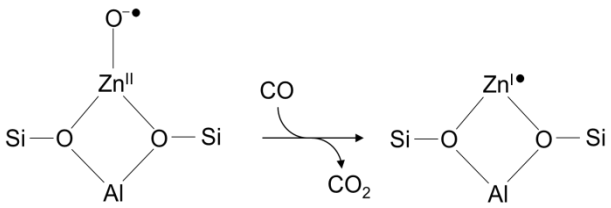

Scheme 1. Scheme of the oxyl-transfer reaction.

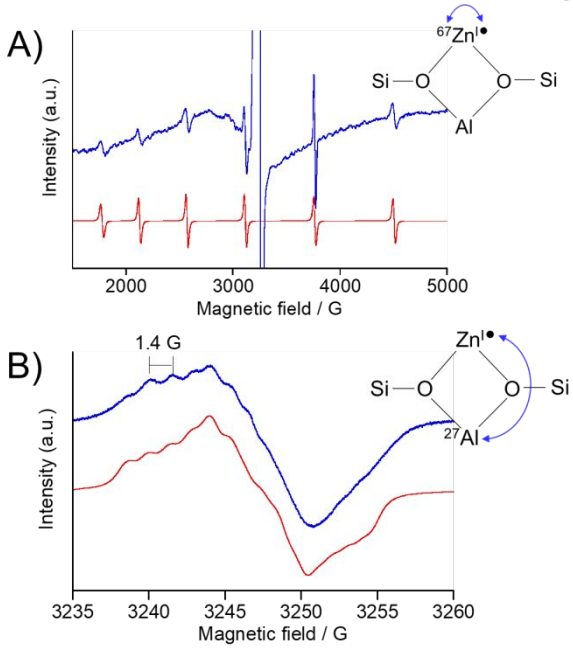

Fig. 2. (A) The hyperfine structure of the natural abundant $^{67}Zn^{I\bullet}$: (blue line) the experimental spectrum in the 1500–5000 G region; (red line) the simulated spectrum of $^{67}Zn^{I\bullet}$ obtained with ESR parameters of g_{xx}= 1.9952, g_{yy}= 1.9982, g_{zz}= 2.0014 and A_{xx}= 537, A_{yy}= 541, A_{zz}= 547 G tensors. (B) The superhyperfine structure of the $Zn^{I\bullet}$ species with the framework ^{27}Al atom: (blue line) the experimental spectrum in the 3235–3260 G region; (red line) the simulation of the experimental spectrum obtained by assuming the g_{xx}= 1.9952, g_{yy}= 1.9982, g_{zz}= 2.0014 and A_{xx}= 1.04, A_{yy}= 1.09, A_{zz}= 1.39 G tensors. All experimental spectra were collected at 4 K.

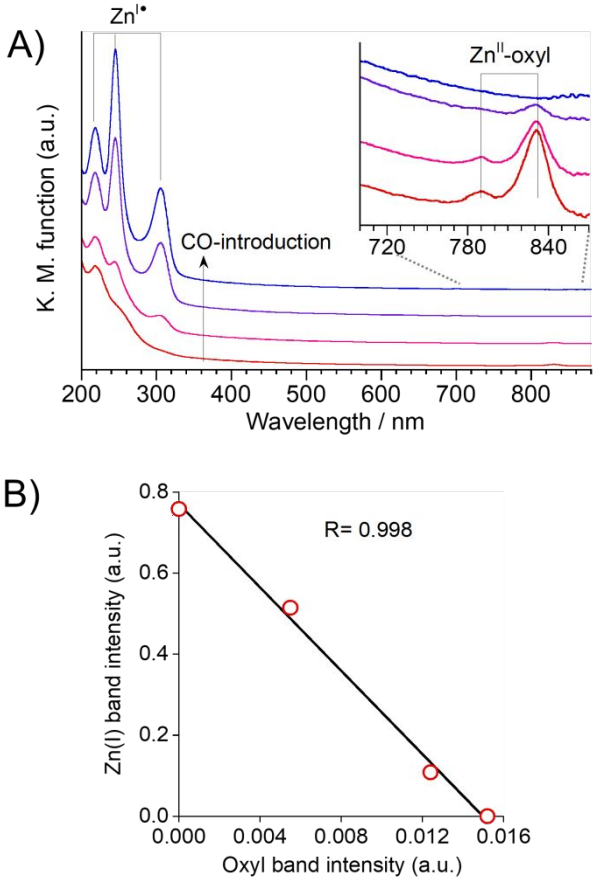

Fig. 3. (A) Change in the UV-Vis-NIR spectra of the sample upon the titration of oxyl with CO (P_e < 0.01 Torr). The 700–870 nm region was enlarged for clearly depicting the vibronic progression of the Zn^{II}–oxyl sites, where the offset of each spectrum was arbitrarily adjusted to make the peaks easier to see. (B) A plot of the intensities of the vibronic progression of the Zn^{II}–oxyl species (832 nm band) and the UV-band derived from the Zn^{I} species (306 nm band). The changes in the intensities of the band at 832 nm and 306 nm upon the reaction with CO were estimated accurately based on the difference spectra that were drawn with reference to the red spectrum shown in **Fig. 3A**.

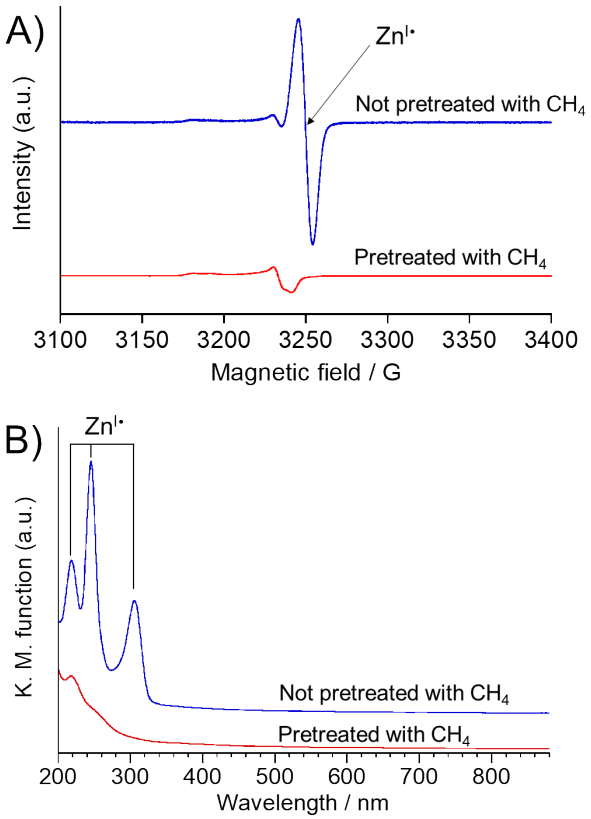

Fig. 4. (A) ESR and (B) UV-Vis-NIR spectra of the samples after the reaction with CO at RT: (blue line) the sample not pretreated with CH_4; (red) the sample pretreated with CH_4 where the oxyl was deactivated through the irreversible reaction with CH_4.

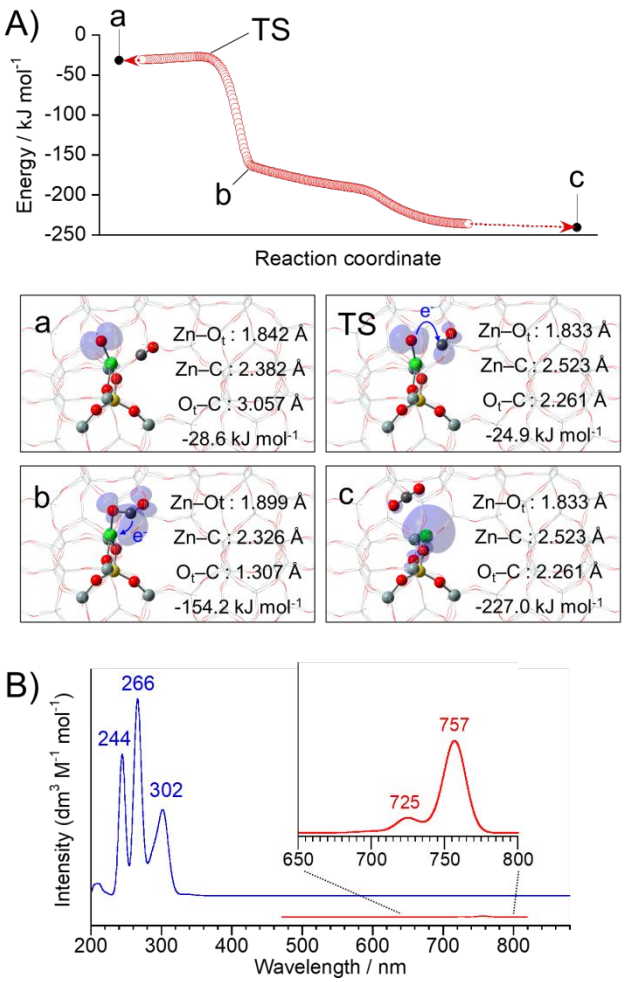

Fig. 5. (A) Computed PES for the oxyl transfer from Zn^{II}–oxyl species to CO. QM/MM calculation was applied for this calculation. The QM region was depicted as ball and stick style, whereas the remaining atoms were drawn as a wireframe style. The selective structural parameters as well as the ZPE-corrected energies were given in the model schemes, where O_t means the terminal oxyl. The computed spin density distributions were depicted as blue surfaces. Legend: green, Zn; black, C; yellow, Al; grey, Si; red, O. (B) Computed UV-Vis-NIR spectra of the DFT cluster models of (red) Zn^{II}–oxyl and (blue) $Zn^{I\bullet}$.

Table 1. Mulliken charges of Zn, O_t, C, and O atoms for the models a, TS, b, and c shown in **Fig. 5A**.

	a	TS	b	c
Zn	0.516	0.544	0.558	0.378
O_t	-0.368	-0.376	-0.298	-0.188
C	0.097	0.063	0.160	0.361
O	0.073	0.051	-0.174	-0.168

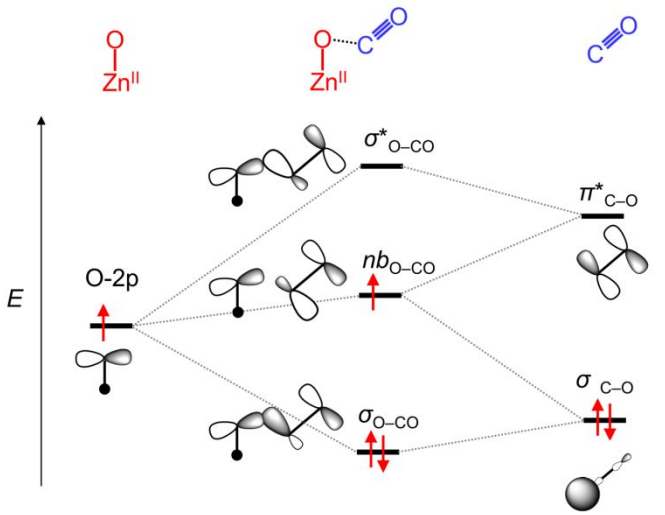

Scheme 2. Schematic molecular orbital diagram representing the orbital interaction between two fragments: Zn^{II}–oxyl (left: singly occupied O-2*p* fragment orbital perpendicular to the Zn^{II}–oxyl bond axis) and CO (right: doubly occupied σ_{C-O} fragment orbital and unoccupied π^*_{C-O} fragment orbital), at the TS coordinate.

Notes and references

1. H. F. Liu, R. S. Liu, K. Y. Liew, R. E. Johnson and J. H. Lunsford, Partial Oxidation of Methane by Nitrous-Oxide over Molybdenum on Silica, *J. Am. Chem. Soc.*, 1984, **106**, 4117–4121.
2. T. Ito and J. H. Lunsford, Synthesis of Ethylene and Ethane by Partial Oxidation of Methane over Lithium-Doped Magnesium Oxide, *Nature*, 1985, **314**, 721–722.
3. T. Ito, J. Wang, C. H. Lin and J. H. Lunsford, Oxidative Dimerization of Methane over a Lithium-Promoted Magnesium Oxide Catalyst, *J. Am. Chem. Soc.*, 1985, **107**, 5062–5068.
4. J. X. Wang and J. H. Lunsford, Characterization of $[Li^+O]$ Centers in Lithium-Doped Magnesium Oxide Catalysts, *J. Phys. Chem.*, 1986, **90**, 5883–5887.
5. J. H. Lunsford, The Catalytic Oxidative Coupling of Methane, *Angew. Chem. Int. Ed.*, 1995, **34**, 970–980.
6. V. Sobolev, K. Dubkov, O. Panna and G. Panov, Selective Oxidation of Methane to Methanol on a FeZSM-5 Surface, *Catal. Today*, 1995, **24**, 251–252.
7. M. Sterrer, T. Berger, O. Diwald and E. Knözinger, Energy Transfer on the MgO Surface, Monitored by UV− Induced H_2 Chemisorption, *J. Am. Chem. Soc.*, 2003, **125**, 195–199.
8. J. S. Woertink, P. J. Smeets, M. H. Groothaert, M. A. Vance, B. F. Sels, R. A. Schoonheydt and E. I. Solomon, A $[Cu_2O]^{2+}$ Core in Cu-ZSM-5, the Active Site in the Oxidation of Methane to Methanol, *Proc. Natl. Acad. Sci. U. S. A.*, 2009, **106**, 18908–18913.
9. X. Chen, Y. Li, X. Pan, D. Cortie, X. Huang and Z. Yi, Photocatalytic Oxidation of Methane over Silver Decorated Zinc Oxide Nanocatalysts, *Nat. Commun.*, 2016, **7**, 12273.
10. B. E. Snyder, P. Vanelderen, M. L. Bols, S. D. Hallaert, L. H. Böttger, L. Ungur, K. Pierloot, R. A. Schoonheydt, B. F. Sels and E. I. Solomon, The Active Site of Low-Temperature Methane Hydroxylation in Iron-Containing Zeolites, *Nature*, 2016, **536**, 317–321.
11. B. E. R. Snyder, M. L. Bols, R. A. Schoonheydt, B. F. Sels and E. I. Solomon, Iron and Copper Active Sites in Zeolites and Their Correlation to Metalloenzymes, *Chem. Rev.*, 2018, **118**, 2718–2768.
12. N. B. Wong, Y. B. Taarit and J. H. Lunsford, Formation of O^- in ZnO from the Dissociation of Adsorbed N_2O, *J. Chem. Phys.*, 1974, **60**, 2148–2151.
13. D. M. Herlihy, M. M. Waegele, X. Chen, C. Pemmaraju, D. Prendergast and T. Cuk, Detecting the Oxyl Radical of Photocatalytic Water Oxidation at an n-$SrTiO_3$/Aqueous Interface Through Its Subsurface Vibration, *Nat. Chem.*, 2016, **8**, 549–555.
14. X. Chen, S. N. Choing, D. J. Aschaffenburg, C. D. Pemmaraju, D. Prendergast and T. Cuk, The Formation Time of Ti–O$^\bullet$ and Ti–O$^\bullet$–Ti Radicals at the n-$SrTiO_3$/Aqueous Interface During Photocatalytic Water Oxidation, *J. Am. Chem. Soc.*, 2017, **139**, 1830–1841.
15. A. Oda, T. Ohkubo, T. Yumura, H. Kobayashi and Y. Kuroda, Identification of a Stable Zn^{II}–Oxyl Species Produced in an MFI Zeolite and Its Reversible Reactivity with O_2 at Room Temperature, *Angew. Chem. Int. Ed.*, 2017, **56**, 9715–9718.
16. A. Oda, T. Ohkubo, T. Yumura, H. Kobayashi and Y. Kuroda, Room-Temperature Activation of the C–H Bond in Methane over Terminal Zn^{II}–Oxyl Species in an MFI Zeolite: A Combined Spectroscopic and Computational Study of the Reactive Frontier Molecular Orbitals and Their Origins, *Inorg. Chem.*, 2019, **58**, 327–338.
17. B. K. Min and C. M. Friend, Heterogeneous gold-based catalysis for green chemistry: low-temperature CO oxidation and propene oxidation. *Chem. Rev.* 2007, ***107***, 2709–2724.
18. X. Xie, Y. Li, Z.-Q. Liu, M. Haruta and W. Shen, Low-temperature oxidation of CO catalysed by Co_3O_4 nanorods. *Nature* 2009, ***458*****,** 746–749.
19. H. J. Freund, G. Meijer, M. Scheffler, R. Schlögl and M. Wolf, CO oxidation as a prototypical reaction for heterogeneous processes. *Angew. Chem. Int. Ed.* 2011, ***50*****,** 10064–10094.
20. G. E. Johnson, R. Mitric, E. C. Tyo, V. Bonacic-Koutecky and A. Castleman Jr, Stoichiometric zirconium oxide cations as potential building blocks for cluster assembled catalysts. *J. Am. Chem. Soc.* 2008, ***130***, 13912–13920.
21. G. E. Johnson, R. Mitric, M. Nössler, E. C. Tyo, V. Bonacic-Koutecky and A. Castleman Jr, Influence of charge state on catalytic oxidation reactions at metal oxide clusters containing radical oxygen centers. *J. Am. Chem. Soc.* 2009, ***131*****,** 5460–5470.
22. J.-B. Ma, B. Xu, J.-H. Meng, X.-N. Wu, X.-L. Ding, X.-N. Li and S.-G. He, Reactivity of atomic oxygen radical anions bound to titania and zirconia nanoparticles in the gas phase: low-temperature oxidation of carbon monoxide. *J. Am. Chem. Soc.* 2013, ***135*****,** 2991–2998.
23. Z.-Y. Li, Z. Yuan, X.-N. Li, Y.-X. Zhao and S.-G. He, CO oxidation catalyzed by single gold atoms supported on aluminum oxide clusters. *J. Am. Chem. Soc.* 2014, ***136*****,** 14307–14313.
24. H. Schwarz, Doping Effects in Cluster-Mediated Bond Activation. *Angew. Chem. Int. Ed.* 2015, ***54*****,** 10090–10100.
25. X. Sun, S. Zhou, L. Yue, M. Schlangen and H. Schwarz, Metal-Free, Room-Temperature Oxygen-Atom Transfer in the N_2O/CO Redox Couple as Catalyzed by $[Si_2O_x]^{\bullet+}$(x= 2–5). *Angew. Chem. Int. Ed.* 2017, ***56*****,** 9990–9993.
26. A. Oda, H. Torigoe, A. Itadani, T. Ohkubo, T. Yumura, H. Kobayashi and Y. Kuroda, Unprecedented Reversible Redox Process in the ZnMFI-H_2 System Involving Formation of Stable Atomic Zn^0, *Angew. Chem. Int. Ed.*, 2012, **51**, 7719–7723.
27. A. Oda, H. Torigoe, A. Itadani, T. Ohkubo, T. Yumura, H. Kobayashi and Y. Kuroda, Mechanism of CH_4 Activation on a Monomeric Zn^{2+}-Ion Exchanged in MFI-Type Zeolite with a Specific Al Arrangement: Similarity to the Activation Site for H_2, *J. Phys. Chem. C*, 2013, **117**, 19525–19534.
28. A. Oda, H. Torigoe, A. Itadani, T. Ohkubo, T. Yumura, H. Kobayashi and Y. Kuroda, An Important Factor in CH_4 Activation by Zn Ion in Comparison with Mg Ion in MFI: The Superior Electron-Accepting Nature of Zn^{2+}, *J. Phys. Chem. C*, 2014, **118**, 15234–15241.
29. S. Stoll, Arthur Schweiger EasySpin, a comprehensive software package for spectral simulation and analysis in EPR, *J. Magn. Reson*., 2006, **178,** 42–55.
30. M. F. Frisch, et al., Gaussian 09, Revision A. 02; *Gaussian*, Inc: Wallingford, CT, 2009.
31. H. Van Koningsveld, J. Jansen and H. Van Bekkum, The Monoclinic Framework Structure of Zeolite H-ZSM-5. Comparison with the Orthorhombic Framework of As-synthesized ZSM-5, *Zeolites*, 1990, **10**, 235–242.
32. P. K. Sajith, Y. Shiota and K. Yoshizawa, Role of Acidic Proton in the Decomposition of NO over Dimeric Cu(I) Active Sites in Cu-ZSM-5 Catalyst: A QM/MM Study, *ACS Catal.*, 2014, **4**, 2075–2085.
33. A. Oda, Y. Mamenari, T. Ohkubo and Y. Kuroda, Spectroscopic Determination of the Site in MFI Zeolite

where Cobalt(I) Performs Two-Electron Reduction of O_2 at Room Temperature, *J. Phys. Chem. C*, 2019, **123**, 17842–17854.

34. A. Oda, T. Nanjo, T. Ohkubo and Y. Kuroda, Experimental Description of Biomimetic Ni^{II}–Superoxo δ-Bond: Franck-Condon Analyses on Its Vibronically-Resolved Spectrum, *J. Phys. Chem. C*, 2020, **124**, 11544−11557.
35. L. Li, G. D. Li, C. Yan, X. Y. Mu, X. L. Pan, X. X. Zou, K. X. Wang and J. S. Chen, Efficient Sunlight-Driven Dehydrogenative Coupling of Methane to Ethane over a Zn^{+}-Modified Zeolite, *Angew. Chem. Int. Ed.*, 2011, **50**, 8299–8303.
36. J. Xu, A. Zheng, X. Wang, G. Qi, J. Su, J. Du, Z. Gan, J. Wu, W. Wang and F. Deng, Room Temperature Activation of Methane over Zn Modified H-ZSM-5 Zeolites: Insight from Solid-State NMR and Theoretical Calculations, *Chem. Sci.*, 2012, **3**, 2932–2940.
37. A. Oda, H. Torigoe, A. Itadani, T. Ohkubo, T. Yumura, H. Kobayashi and Y. Kuroda, Success in Making Zn^{+} from Atomic Zn^{0} Encapsulated in an MFI-Type Zeolite with UV Light Irradiation*, J. Am. Chem. Soc.*, 2013, **135**, 18481–18489.
38. G. Qi, J. Xu, J. Su, J. Chen, X. Wang and F. Deng, Low-Temperature Reactivity of Zn^{+} Ions Confined in ZSM-5 Zeolite Toward Carbon Monoxide Oxidation: Insight from in situ DRIFT and ESR Spectroscopy, *J. Am. Chem. Soc.*, 2013, **135**, 6762–6765.
39. A. Oda, T. Ohkubo, T. Yumura, H. Kobayashi and Y. Kuroda, Synthesis of an Unexpected $[Zn_2]^{2+}$ Species Utilizing an MFI-Type Zeolite as a Nano-Reaction Pot and Its Manipulation with Light and Heat, *Dalton Trans.*, 2015, **44**, 10038–10047.
40. E. Morra, G. Berlier, E. Borfecchia, S. Bordiga, P. Beato and M. Chiesa, Electronic and Geometrical Structure of Zn^{+} Ions Stabilized in the Porous Structure of Zn-Loaded Zeolite H-ZSM-5: A Multifrequency CW and Pulse EPR Study, *J. Phys. Chem. C*, 2017, **121**, 14238–14245.
41. E. Morra, M. Signorile, E. Salvadori, S. Bordiga, E. Giamello and M. Chiesa, Nature and Topology of Metal–Oxygen Binding Sites in Zeolite Materials: ^{17}O High-Resolution EPR Spectroscopy of Metal-Loaded ZSM-5, *Angew. Chem. Int. Ed.*, 2019, **58**, 12398–12403.
42. F. F. Popescu and V. V. Grecu, EPR Study of Zn^{+} in CALCITE, *Solid State Commun*., **1973,** 13, 749–751.
43. K. Kobayashi, H. Ohtsu, T. Wada and K. Tanaka, Ruthenium Oxyl Radical Complex Containing o-Quinone Ligand Detected by ESR Measurements of Spin Trapping Technique, *Chem. Lett.*, 2002, **31**, 868–869.
44. K. Kobayashi, H. Ohtsu, T. Wada, T. Kato and K. Tanaka, Characterization of a Stable Ruthenium Complex with an Oxyl Radical, *J. Am. Chem. Soc.*, 2003, **125**, 6729–6739.
45. E. Poverenov, I. Efremenko, A. I. Frenkel, Y. Ben-David, L. J. W. Shimon, G. Leitus, L. Konstantinovski, J. M. L. Martin and D. Milstein, Evidence for a Terminal Pt(iv)-Oxo Complex Exhibiting Diverse Reactivity, *Nature*, 2008, **455**, 1093–1096.
46. Y. Shimoyama, T. Ishizuka, H. Kotani, Y. Shiota, K. Yoshizawa, K. Mieda, T. Ogura, T. Okajima, S. Nozawa and T. Kojima, A Ruthenium (III)–Oxyl Complex Bearing Strong Radical Character, *Angew. Chem.*, 2016, **55**, 14041−14045.
47. J. Amtawong, D. Balcells, J. Wilcoxen, R. C. Handford, N. Biggins, A. I. Nguyen, R. D. Britt and T. D. Tilley, Isolation and Study of Ruthenium–Cobalt Oxo Cubanes Bearing a High-Valent, Terminal Ru^{V}–Oxo with Significant Oxyl Radical Character, *J. Am. Chem. Soc.*, 2019, **141**, 19859–19869.
48. D. Delony, M. Kinauer, M. Diefenbach, S. Demeshko, C. Würtele, M. C. Holthausen and S. Schneider, A Terminal Iridium Oxo Complex with a Triplet Ground State, *Angew. Chem. Int. Ed.*, 2019, **58**, 10971–10974.
49. Y. Shimoyama and T. Kojima, Metal–Oxyl Species and Their Possible Roles in Chemical Oxidations, *Inorg. Chem*, 2019, **58**, 9517–9541.

TOC Graphic

We demonstrated that the Zn^{II}–oxyl bond specifically created by the zeolite lattice ligation has a capability for transferring the oxyl to CO even at 150 K with the generation of a single $Zn^{I\bullet}$ species.